

Numerical Simulation of Dynamic Mechanical Properties of Porous Concrete Fabricated with the SAP

* Junru Ren, ** Zhiping Deng, *** Hua Cheng, **** Lin Zhou, ***** Xinhao Zheng

* Department of Civil Engineering, Logistical Engineering University, Chongqing 401311, China,
(danielgy@aliyun.com)

** Department of Civil Engineering, Logistical Engineering University, Chongqing 401311,
China;

Technology Brigade of Aerospace Engineering, Beijing 100192, China

*** Department of Civil Engineering, Logistical Engineering University, Chongqing 401311,
China

**** Department of Civil Engineering, Logistical Engineering University, Chongqing 401311,
China

***** Department of Civil Engineering, Logistical Engineering University, Chongqing 401311,
China

Abstract

The superabsorbent polymer (SAP) was utilized to fabricate a new porous concrete with millimetre-size inner pores. To investigate its potential application in military shelters, this paper conducts an SHPB test based on the ABAQUS to numerically simulate dynamic mechanical properties of the porous concrete, including stress wave propagation, lateral inertia confinement effect and end face friction effect. The test results revealed the variation law of lateral confinement effect with strain rate or porosity, and distinguished the strength gain induced by the two lateral confinement effects from the strain-rate effect. Moreover, the author studied the propagation of six triangle stress waves through different pressure bars, and analysed the attenuation law and dispersion effect in porous concrete.

Key words

SAP, Porous concrete, Lateral confinement effect, Stress wave, Propagation, Strain-rate effect, Split-hopkinson pressure bar (SHPB) test.

1. Introduction

Superabsorbent polymer (SAP) powder has been widely used as an additive to reduce dry shrinkage of concrete [1-3]. Cheng et al. [4] pioneered the use of pre-soaked saturated SAP and mortar to fabricate a new porous concrete with spherical millimetre-size inner pores [5-7]. The porous structure boosts the adsorption of energy and wave and holds promise for potential application in military shelters. However, the dynamic mechanical properties of the unconventional porous concrete have not been comprehensively studied. Only Deng et al. [8] experimentally investigated its compressive behaviour under high strain-rate loads on the Split-Hopkinson pressure bar (SHPB). The investigation reveals that the porous concrete is sensitive to high strain rate as its dynamic strength increase factor ($DIF-f_c$) improved with the strain rate [9].

The stress wave propagation, an indicator of wave absorbing ability, is particularly complex in the porous concrete, for the spatial reticulated shell structure contains many free shell surfaces and spatially distributed internal stress. The theoretical analysis is further complicated by the nonlinear properties in the constitutive model of the porous concrete, such as the global or local plastic properties [8-9], especially when stressed to plastic region. Meanwhile, the strain-rate effect of the porous concrete derived from the SHPB test is partly attributed to the lateral confinement effect, including lateral inertia confinement effect and end face friction effect [10-16].

To acquire more accurate stress wave propagation and material parameters of the strain-rate effect, it is necessary to carry out numerical simulation by the finite-element method. Based on the ABAQUS platform and the extended Drucker-Prager model [17-20], this paper conducts an SHPB test to investigate the stress wave propagation, lateral inertial confinement effect and end-face friction effect of the porous concrete under impact load.

2. Numerical Model and Method

2.1 Simplified SHPB Device

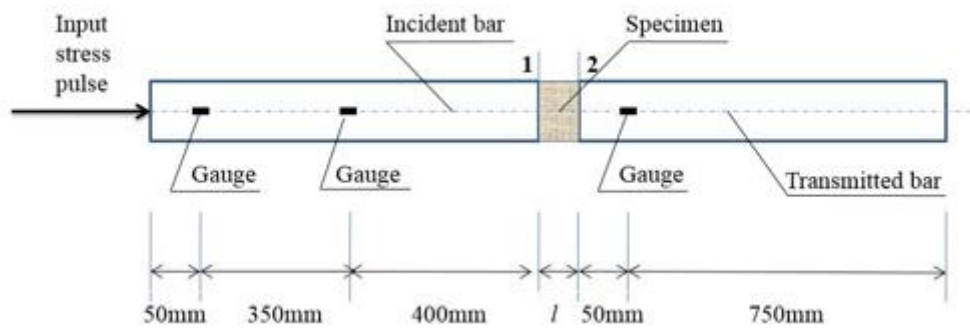


Fig.1. Schematic Diagram of Simplified SHPB Test

As shown in Figure 1, the numerical model consists of the same components with the actual SHPB test device. However, it was simplified to ease the computing load, reduce the deviation from the test results, and obtain the full waveform. The conical incident bar and the transmitted bar were reduced to uniform and square cross-section bars. After modification, the two bars were of the same size with the length shortened to 800mm. Meanwhile, the cylinder specimens were simplified to same-size rectangles.

50mm long specimens were used ($l=50\text{mm}$) to investigate the lateral confinement effect, and a longer specimen ($l=150\text{mm}$) was adopted to accommodate a complete stress wave in the analysis of stress wave propagation. The friction coefficient between pressure bar and specimen was set to 0, neglecting friction effect.

2.2 Material Model

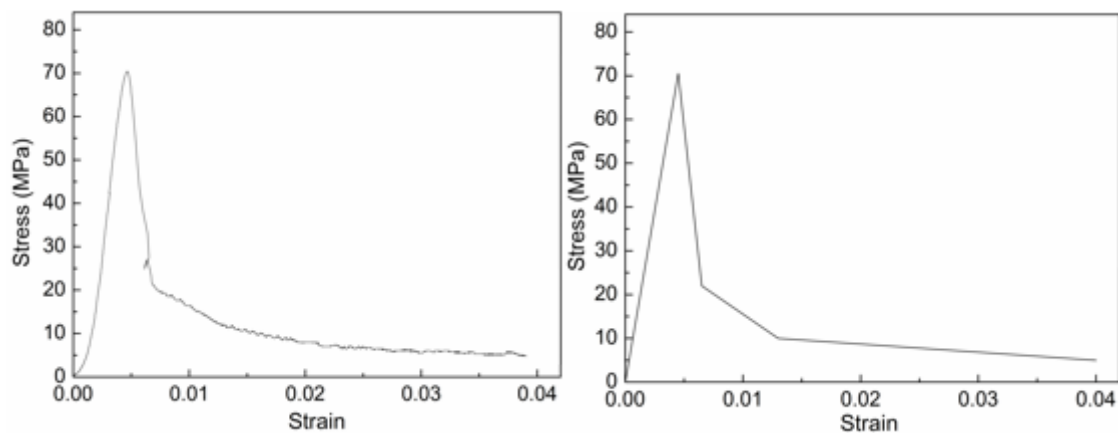
2.2.1 Material model for mortar

The SHPB test on the porous concrete was conducted at different porosities of 10%, 20%, 30% and 40% and under quasi-static load or dynamic loads at three strain-rate levels (70/s, 100/s and 140/s). The test data were listed in Table 1. The uniaxial compressive stress-strain curve under quasi-static load of the mortar is shown in Figure 2 (a). The simplified version of the curve (Figure 2(b)) was inputted to the extended Drucker-Prager model of ABAQUS, seeking to depict the stress-strain relationship and the correlation with hydrostatic pressure.

Tab.1. Mechanical properties of porous concrete under quasi-static and impact load

| Theoretical porosity (%) | Real porosity (%) | Quasi-static strength (MPa) | Average strain rate (/s) | Compressive strength (MPa) | DIF- f_c |
|--------------------------|-------------------|-----------------------------|--------------------------|----------------------------|------------|
| 10 | 9.5 | 53.6 | 79.7 | 95.4 | 1.78 |
| | | | 107.6 | 102.4 | 1.91 |

| | | | | | |
|----|------|------|-------|-------|------|
| | | | 140.2 | 108.8 | 2.03 |
| | | | 68.2 | 68.2 | 1.80 |
| 20 | 19.3 | 37.9 | 100.0 | 74.7 | 1.97 |
| | | | 126.9 | 80.3 | 2.12 |
| | | | 70.5 | 40.1 | 1.92 |
| 30 | 27.8 | 20.9 | 104.7 | 45.1 | 2.16 |
| | | | 142.7 | 50.8 | 2.43 |
| | | | 72.1 | 30.7 | 1.97 |
| 40 | 38.7 | 15.6 | 101.5 | 36.0 | 2.31 |
| | | | 141.5 | 40.2 | 2.58 |



(a) Quasi-static uniaxial stress-strain curve of the mortar

(b) Simplified quasi-static uniaxial stress-strain curve of the mortar

Fig.2. Quasi-static uniaxial stress-strain curve

2.2.2 Material model for pressure bars

Derived from the classic Drucker-Prager elasto-plastic model [17] in the ABAQUS, the extended Drucker-Prager model can simulate the strength gain of concrete with the increase in confinement pressure, as it is capable of depicting the stress flow of concrete, which is resulted from the internal friction and associated with the confining pressure. The model can also calculate the deformation in large-deformation dynamics, including strain hardening and strain softening.

According to Table 2, four kinds of pressure bars were applied in the test. The first three of them, denoted as pressure bars 1, 2 and 3, were made of mortar, steel fibre reinforced concrete (SFRC) and corundum concrete, respectively. Pressure bar 1 was mainly used to study the waveform change through the porous concrete specimen. In light of the extensive use of the SFRC and corundum concrete in protective engineering, pressure bars 2 and 3 were relied on to

examine the stress wave propagation in a sandwich structure with the porous concrete as the interlayer. Pressure bar 4 was a normal steel bar utilized to explore the lateral confinement effect.

A linear elastic model was selected for pressure bar 1. The density, elastic modulus and Poisson's ratio were configured in accordance with the mortar. For pressure bars 2 and 3, the same linear elastic model was applied with parameters obtained from the existing studies.

Figure 2 displays the mechanical parameters of the mortar under uniaxial compression. Some parameters in the extended Drucker-Prager model, namely the friction angle β and dilatancy angle ψ , were determined by triaxial test. In the rock triaxial test system, the compressive mechanical behaviours were examined under uniform confining pressures ($\sigma_2=\sigma_3$) of 14MPa, 28MPa and 42MPa. The stress relationship $\sigma_1-\sigma_3$, axial strain ε_1 , lateral strain ε_3 and volume strain $\varepsilon_v=\varepsilon_1+2\varepsilon_3$ were recorded, laying the basis for deriving the relationship between additional stress σ_1 and ε_v . After the fitting with linear equation β was deduced as 46° from the test data. Bertholf et al. [22] reported that the effect of ψ on the SHPB test result is negligible. Thus, the value of ψ was deemed as equal to β . Namely, the slant plane parameter K equals 1, signifying the use of the associated flow rule.

Tab.2. Material properties involved in the numerical model

| Test | Name | Density (kg/m ³) | Elastic modulus (GPa) | Poisson ratio | Compressive strength (MPa) | β | ψ | K |
|---------------------|--------|------------------------------|-----------------------|---------------|----------------------------|------------|------------|-----|
| Propagation | Bar 1 | 2172 | 24.2 | 0.21 | — | — | — | — |
| | Bar 2 | 2700 | 47.5 | 0.18 | — | — | — | — |
| | Bar 3 | 3800 | 400 | 0.3 | — | — | — | — |
| Lateral confinement | Bar 4 | 7850 | 210 | 0.3 | 400 | — | — | — |
| — | Mortar | 2172 | 24.2 | 0.21 | 70.5 | 46° | 46° | 1 |

In addition, some parameters correlated with the strain-rate sensitivity caused by material itself should be introduced to amend the model in stress wave propagation analysis. These parameters can be derived from results in section 3. The formula suggested by CEB [14] is used to fit the function describing the strain-rate effect caused by material itself, by which the function with φ and γ and porosity V can be established as:

$$\varphi = \frac{0.5804}{1 + e^{1.625 - 0.0568V}} \quad (1)$$

$$\gamma = 1.69 \times 10^{-4} V^2 - 0.0134V + 0.2684 \quad (2)$$

According to equations (1) and (2), the parameter values of mortar ($V=0$) can be deduced as $\varphi=0.095$ and $\gamma=0.268$. This means, the strain-rate effect is solely caused by the material itself. Thus, the variation of dynamic strength increase factor (DIF) caused by mortar itself and the strain rate can be obtained by equation (3), as recommended by CEB [14].

$$DIF - f_c = \frac{f_c}{f_{cs}} = \begin{cases} (\dot{\epsilon} / \dot{\epsilon}_s)^{1.026\alpha_s} & \dot{\epsilon} \leq 30 / s \\ 0.268(\dot{\epsilon} / \dot{\epsilon}_s)^{0.095} & \dot{\epsilon} \geq 30 / s \end{cases} \quad (3)$$

The introduction of equation (3) makes it possible to simulate the dynamic mechanical behaviours of porous concrete on the extended Drucker-Prager model. In order to avoid possible errors, φ and γ were calibrated against the stress-strain curves through trial calculations and tabulated in Table 3.

Tab.3. Parameter φ and γ of mortar

| Porosity of the concrete (%) | φ | γ |
|------------------------------|-----------|----------|
| 10 | 1.03 | 2.38 |
| 20 | 1.12 | 2.22 |
| 30 | 1.19 | 2.13 |
| 40 | 1.25 | 1.97 |

2.2.3 Mesh generation

As mentioned in Section 2.1, the shapes of pressure bars and specimens were simplified to improve the mesh quality. According to trial calculations, the mesh quality around the pores directly bears on the precision of dynamic calculation. Thus, the structured mesh technology and C3D8R element (three-dimensional eight-node brick element with reduced integration) were applied to eliminate the hourglass effect. Then, a one-fourth model with symmetrical boundary conditions was established based on the symmetry. The related parameters for specimen with different porosities in Table 4.

Tab.4. Parameter of the finite element model for specimen

| Bore diameter (mm) | Theoretical porosity (%) | Actual porosity (%) | Simulated porosity (%) | Size of the cell (mm) | Bore number | Unit number |
|--------------------|--------------------------|---------------------|------------------------|-----------------------|-------------|-------------|
| | | | | | | |

| | | | | | | |
|---|----|------|------|----------------------|-----|--------|
| | 10 | 9.5 | 9.5 | 8.7656×8.7656×8.7656 | 196 | 84672 |
| 5 | 20 | 19.3 | 19.7 | 7.000×6.8930×6.8930 | 405 | 88290 |
| | 30 | 27.8 | 29.2 | 5.9033×6.1667×6.1667 | 600 | 76800 |
| | 40 | 38.7 | 38.5 | 5.700×5.4624×5.4624 | 792 | 101376 |

3. Analysis of Lateral Confinement Effect

3.1 Input Stress Pulse

Based on the test results [8-9], the recorded incident stress waves were loaded in the numerical model as input stress pulse in the numerical model. Typical incident stress waves are shown in Figure 3.

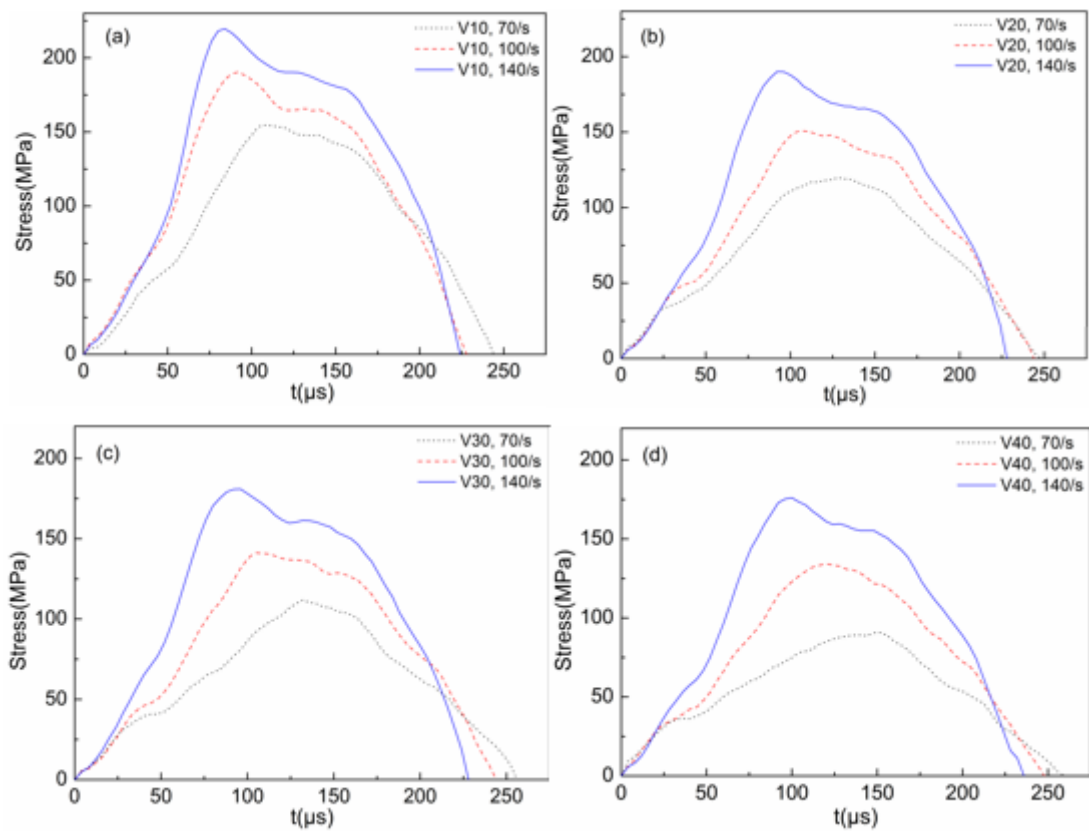


Fig.3. Input Stress Wave Pulses

3.2 Results and Discussion

3.2.1 Lateral confinement effect

Figures 4 and 5 illustrate the increment variation of reconstructed compressive strength $\Delta f_{c,lat}$ with porosities and strain rates, respectively. Figures 6 and 7 display the relationship between the peak hydrostatic pressure p_c of the specimens and porosity or strain rate.

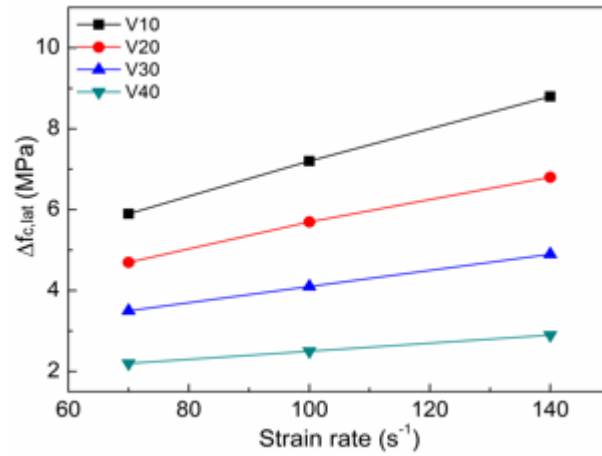


Fig. 4 Variation of $\Delta f_{c,lat}$ with strain rate

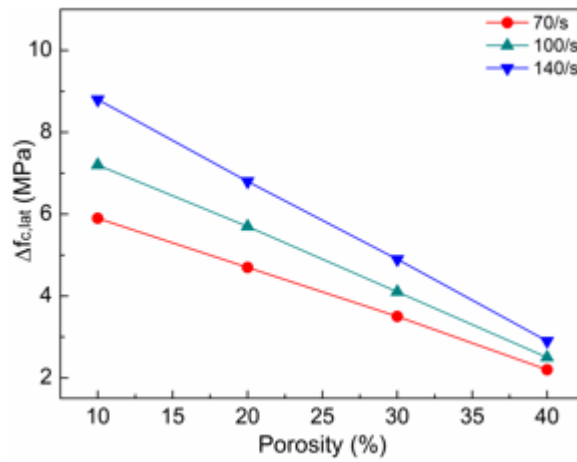


Fig. 5 Variation of $\Delta f_{c,lat}$ with porosity

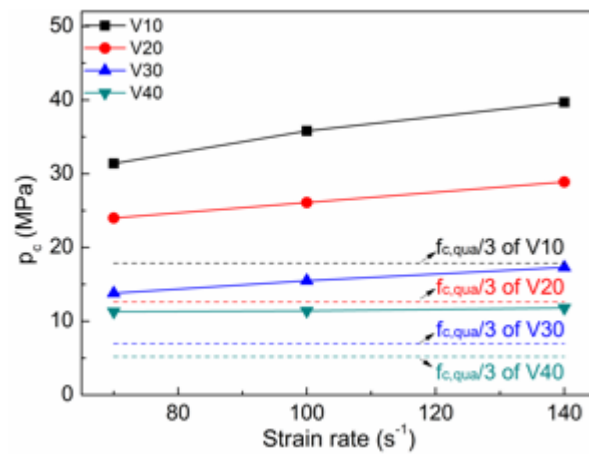


Fig.6. Variation of p_c with strain rate

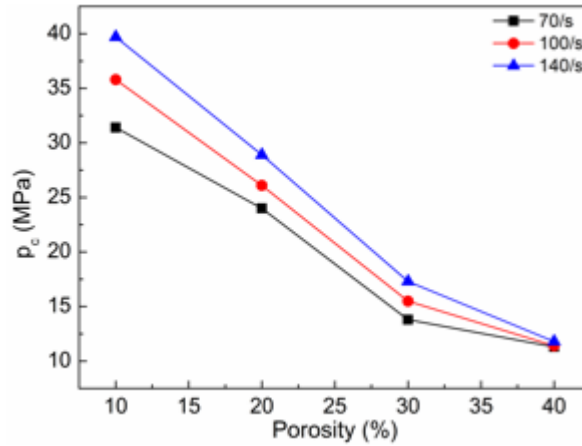


Fig. 7 Variation of p_c with porosity

According to Figures 4 and 5, $\Delta f_{c,lat}$ decreased with the increase in porosity under the same strain rate. This reveals that the growth of compressive strength is largely attributable to the material itself, considering the weakening of the lateral inertia effect by the pores in concrete. Meanwhile, $\Delta f_{c,lat}$ increased with the strain rate when the porosity remained constant. Besides, low porosity specimens exhibited larger $\Delta f_{c,lat}$, indicating that $\Delta f_{c,lat}$ is more sensitive to strain rate at a low porosity. Figure 6 and Figure 7 demonstrate that p_c decreased with the increase of porosity under the same strain rate, and increased with the strain rate when the porosity remained constant. Hence, $\Delta f_{c,lat}$ and p_c have a similar trend with varying porosity or strain rate.

The four dotted lines in Figure 6 stands for 1/3 of the quasi-static compressive strength $f_{c,qua}$ of the porous concrete. It is observed that p_c surpassed the 1/3 and approximated the 1/2 of $f_{c,qua}$ in all conditions. The previous researches [20-21] have shown that, if p_c is higher than 1/3 of the quasi-static uniaxial compressive strength, the other two principal stresses σ_2 and σ_3 cannot be equal to zero, the inside of specimen must be under non-uniaxial stress, and the significant inertia effect may confine the lateral deformation. According to the extended Drucker-Prager model, the uniaxial compressive strength of concrete material is positively correlated with hydrostatic pressure. Therefore, the strain-rate effect on compressive strength in the SHPB test on porous concrete is not solely induced by the dynamic response of the material, but is also due partly to the lateral inertial confinement effect under impact load, which is difficult to be ruled out in experiment.

3.2.2 End face friction effect

Based on the SHPB test results, Bertholf et al. [22] numerically simulated the influence of friction between specimen and pressure bar, and pointed out that the end face friction effect can be eliminated if the interface is well lubricated. Nevertheless, the conclusion only applies to metal specimens, that often have a smaller friction coefficient than that of concrete. Therefore, the end face friction effect cannot be completely excluded despite lubrication measures.

In this research, the friction coefficient μ of the contact surface was set to 0.05, 0.1, 0.2, 0.1 and 0.2 respectively. The abovementioned model was applied to calculate the reconstructed stress-strain curves of different porous concrete specimens at various strain-rate levels. In reference to these curves, the author obtained the reconstructed compressive strength $f_{c,lat-\mu}$, which reflects how lateral inertia confinement and end face friction affect the compressive strength. The increment $\Delta f_{c,lat-\mu}$ was derived by subtracting $f_{c,lat}$ from $f_{c,lat-\mu}$, and used to express the impact from end fact friction. The fluctuation in $\Delta f_{c,lat-\mu}$ is exhibited in Figure 8.

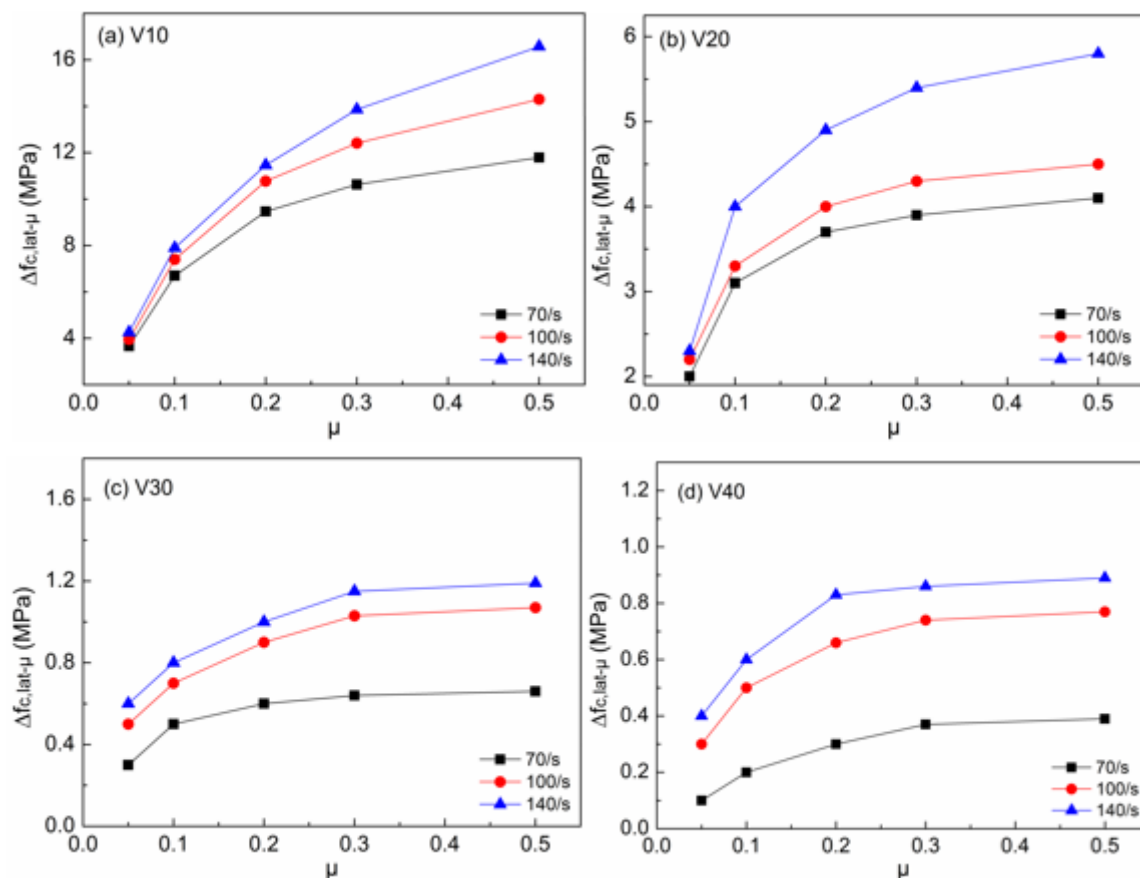


Fig.8. Variation of $\Delta f_{c,lat-\mu}$ with friction coefficient

It can be seen in Figure 8 that the $\Delta f_{c,lat-\mu}$ of all specimens were greater than zero, indicating that the effect of end face friction on the compressive strength should not be neglected. No

surprisingly, the $\Delta f_{c,lat-\mu}$ resulted from end face friction increased with the friction. In the meantime, the growth of $\Delta f_{c,lat-\mu}$ accelerated after the friction coefficient fell below 0.2, and gradually slowed down after the coefficient surpassed 0.2. At the given friction coefficient and porosity, the $\Delta f_{c,lat-\mu}$ increased with the strain rate, revealing that the end face friction has a great impact on the compressive strength under the impact load. The impact was more pronounced for low-porosity specimens after the friction coefficient exceeded 0.2. The above results call for friction reduction to guarantee the accuracy of the SHPB test.

3.2.3 Strain rate effect of the material itself

The dynamic strength increase factor $DIF-f_c$ was deduced from the SHPB test as:

$$DIF-f_c = f_c / f_{cs} = (\Delta f_c + f_{cs}) / f_{cs} \quad (4)$$

Where Δf_c is the increment of dynamic compressive strength under the joint action of the lateral inertia confinement, the end face friction and the strain-rate effect of the material itself; f_{cs} is the compressive strength under quasi-static load.

The increment of dynamic compressive strength $\Delta f_{c,r}$ caused by the material itself can be expressed as below if it is not correlated with $\Delta f_{c,lat-\mu}$ or Δf_c .

$$\Delta f_c = \Delta f_{c,r} + \Delta f_{c,lat-\mu} \quad (5)$$

Substitute equation (5) into equation (4) and we have:

$$DIF-f_c = (\Delta f_{c,r} + \Delta f_{c,lat-\mu} + f_{cs}) / f_{cs} \quad (6)$$

Ignoring the strain-rate effect of the material itself, the dynamic strength increase factor was modified as $DIF-f_{c,lat-\mu}$, which only hinges on the two lateral confinement effects. Thus, the dynamic strength increase factor $DIF-f_{c,r}$ can be expressed as equation (7):

$$DIF-f_{c,r} = DIF-f_c - DIF-f_{c,lat-\mu} \quad (7)$$

According to Literature [18], it is possible to reduce the friction coefficient between specimen and steel pressure bar to about 0.1 in the SHPB test. Taking the coefficient as 0.1, i.e. $\mu=0.1$, the author computes the value of $DIF-f_{c,lat-\mu}$ and $DIF-f_{c,r}$ based on the $\Delta f_{c,lat-\mu}$ in Figure 8.

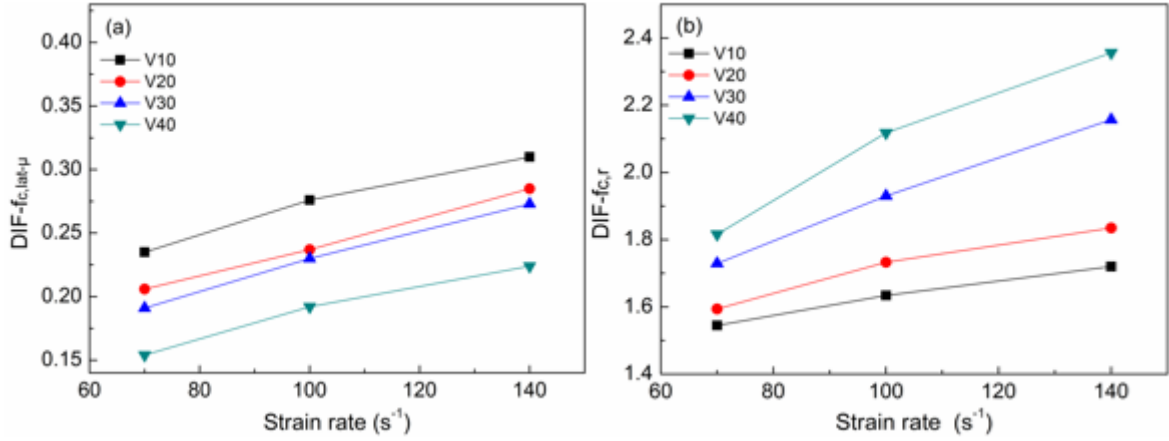


Fig.9. $DIF-f_{c,lat-\mu}$ and $DIF-f_{c,r}$ of specimens

As shown in Figure 9, the $DIF-f_{c,r}$ demonstrated obvious sensitivity to strain-rate and increased with concrete porosity, and the $DIF-f_{c,lat-\mu}$ also grew along with porosity. The results show that the two lateral confinement effects are more evident in low porosity specimens. Under the same strain rate, the $DIF-f_{c,r}$ increased with the rise of porosity, revealing that high porosity specimens have more significant strain-rate effect of the material itself. The conclusion echoes the SHPB test results [8-9]. The variation in the strain-rate effect of the material itself was fitted by equation (8). The parameter values are listed in Table 5. Judging by the fitted curves in Figure 10, it is learned that the $DIF-f_{c,r}$ and relative strain rate $\dot{\epsilon} / \dot{\epsilon}_s$ maintain a double logarithmic, linear relationship.

$$DIF-f_{c,r} = b \left(\frac{\dot{\epsilon}}{\dot{\epsilon}_s} \right)^a \quad (8)$$

Tab.5. Parameter of the fittig equation

| Theoretical porosity (%) | <i>a</i> | <i>b</i> |
|--------------------------|----------|----------|
| 10 | 0.1499 | 0.1548 |
| 20 | 0.0746 | 0.2034 |
| 30 | 0.0141 | 0.3190 |
| 40 | 0.0063 | 0.3761 |

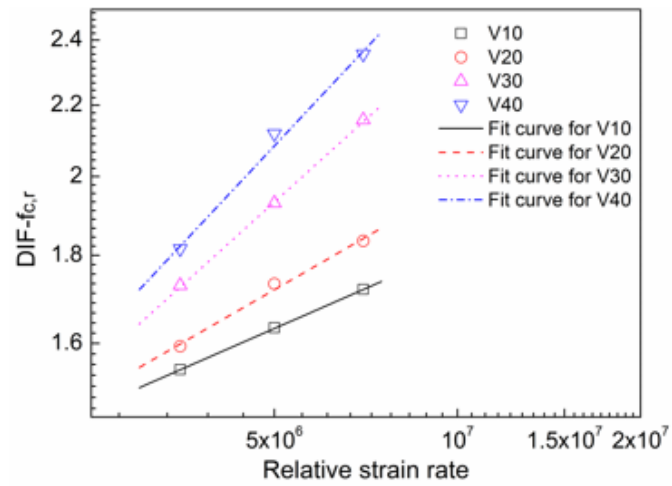


Fig.10. Variation of DIF- $f_{c,r}$ with relative strain rate

4. Stress Wave Propagation Analysis

4.1 Input Stress Wave

As shown in Figure 11, the incident stress waves were triangle waves with a pulse time of $40\mu\text{s}$ or $80\mu\text{s}$ and a peak stress of 5MPa, 15MPa or 25MPa.

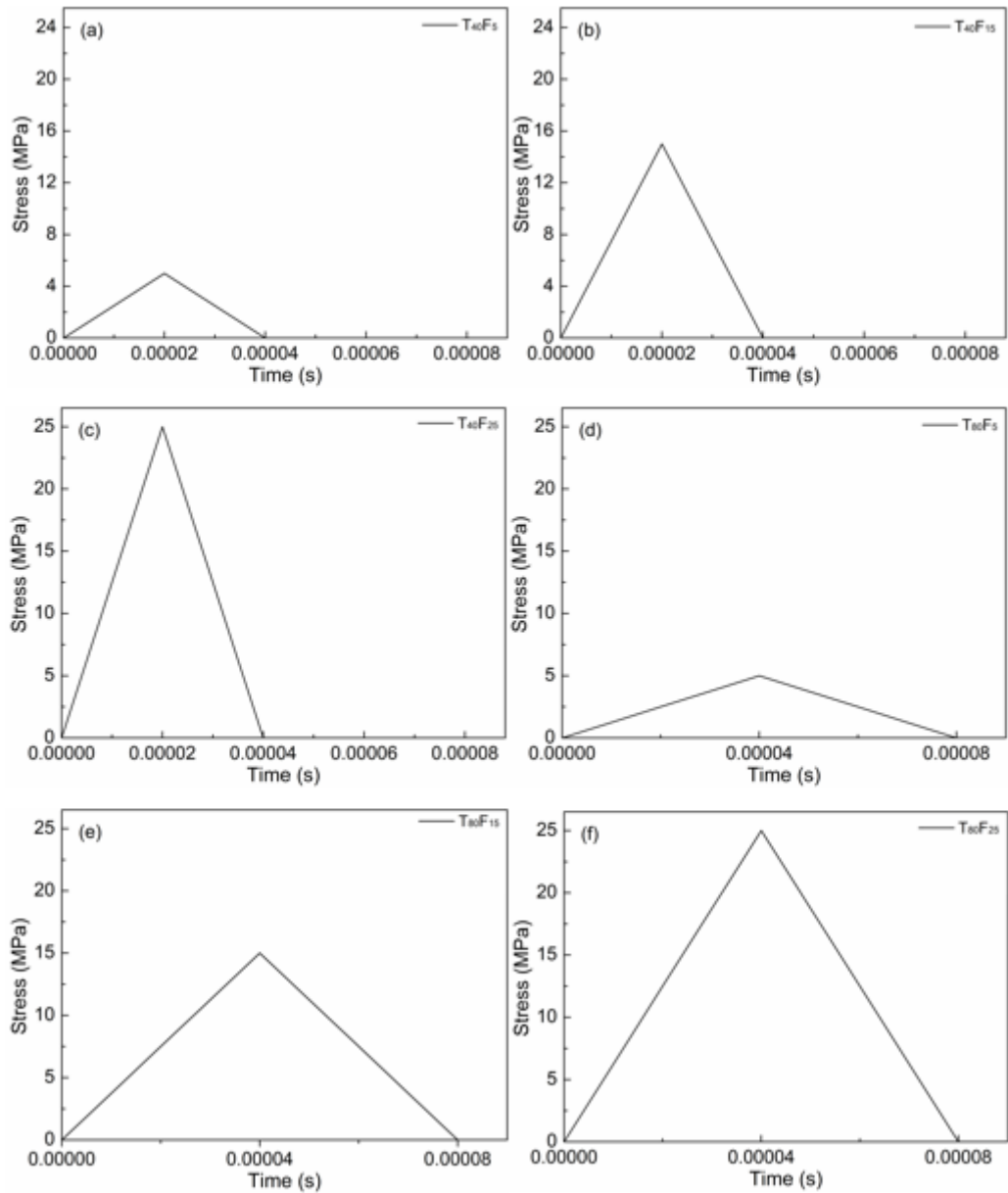


Fig.11. Incident stress pulses (T-pulse time of incident stress wave, F-peak stress)

4.2 Results of Stress Wave Propagation

In total, 6 incident waves were created based on the different pulse times (T) and peak stresses (F). With 3 pressure bars and 4 kinds of porous concrete with various porosities (V), the author probed into 40 scenarios, and recorded the 24 transmitted stress waves below.

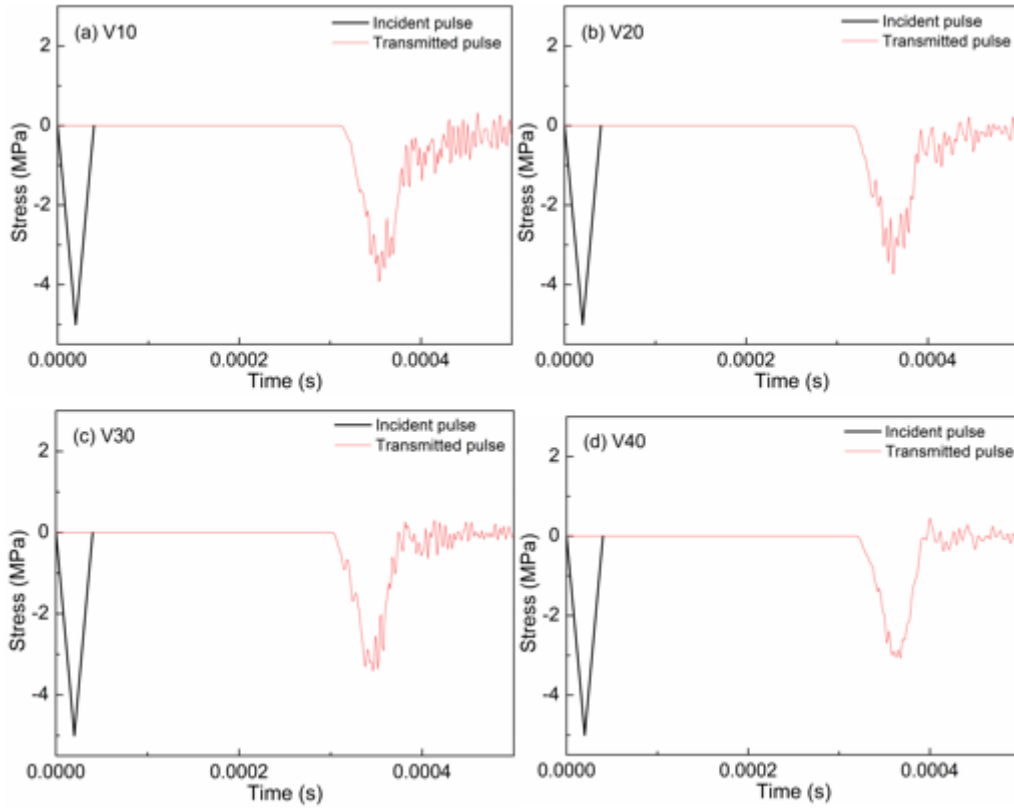


Fig.12. Transmitted stress pulse for stress wave T_{40F5} through pressure bar1

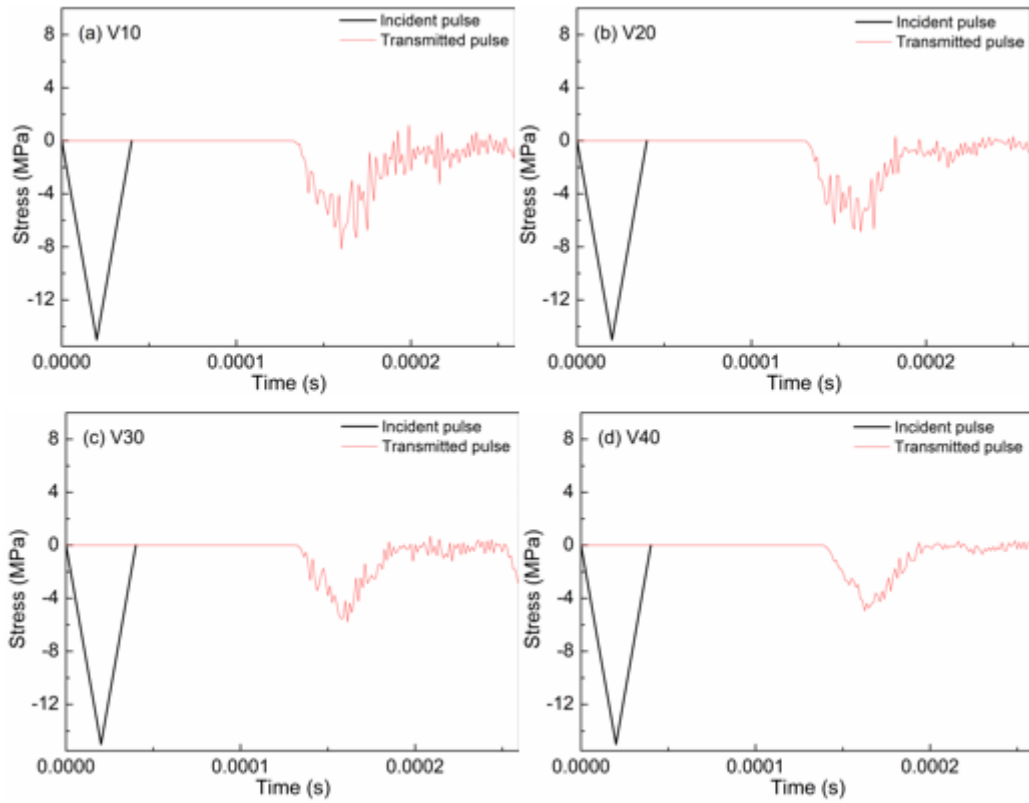


Fig.13. Transmitted stress pulse for stress wave T_{40F15} through pressure bar3

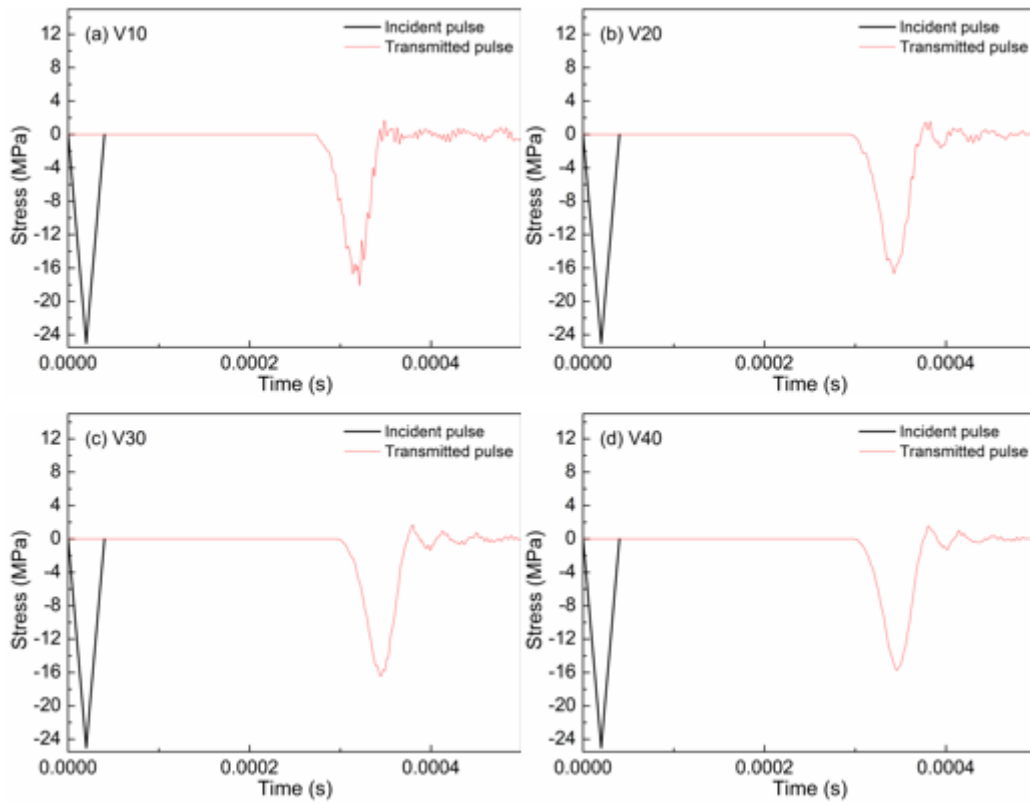


Fig.14. Transmitted stress pulse for stress wave $T_{40}F_{25}$ through pressure bar1

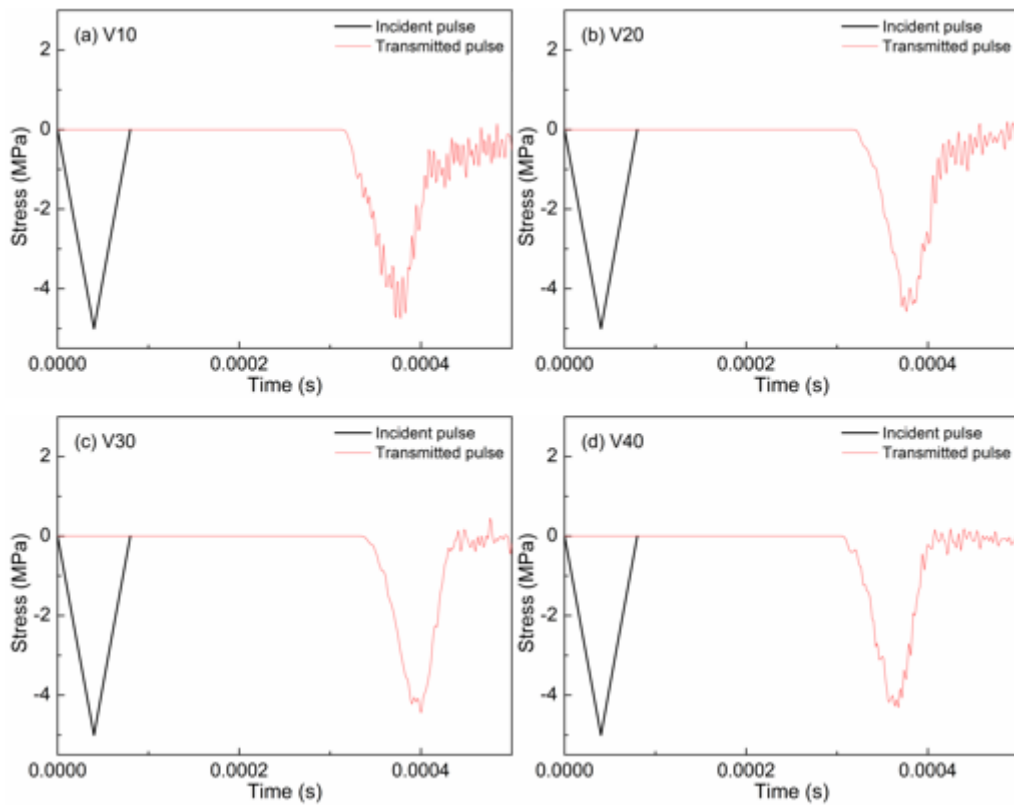


Fig.15. Transmitted stress pulse for stress wave $T_{80}F_5$ through pressure bar1

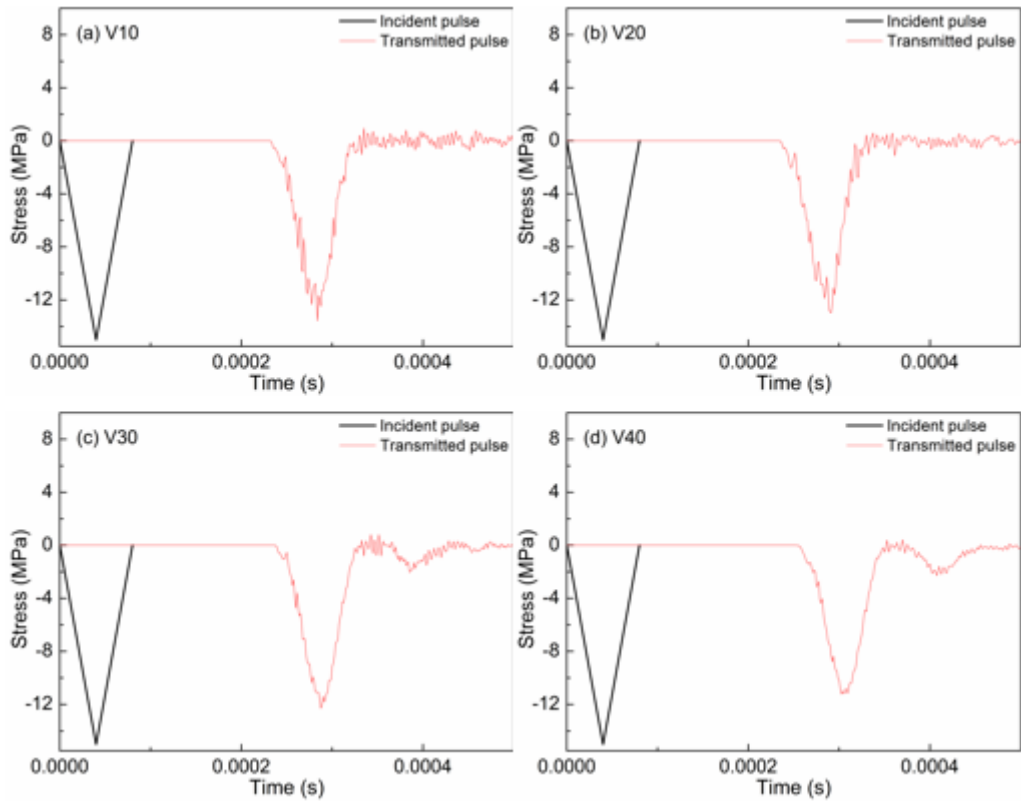


Fig.16. Transmitted stress pulse for stress wave T_{80F15} through pressure bar2

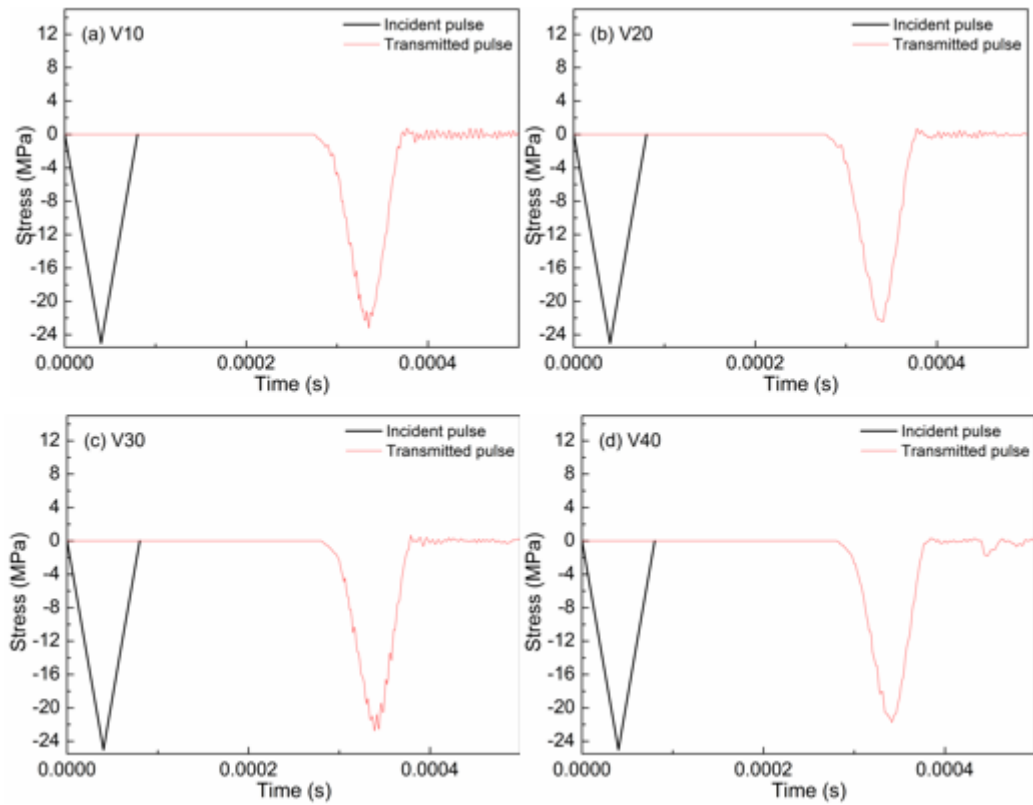


Fig.17. Transmitted stress pulse for stress wave T_{80F25} through pressure bar1

4.3 Discussions

4.3.1 Effect of porosity on transmission ratio

Figure 18 depicts transmission ratio σ_T/σ_I (i.e. the ratio of transmitted stress to incident stress) in all scenarios. The transmission ratios on pressure bar 1 evidences the wave attenuation effect of porous concrete itself under impact load. While the transmission ratio always stayed below 1 and decreased with increasing porosity, the incident stress waves with shorter pulse time resulted in significantly smaller transmission ratios. It is also concluded that the porous concrete evidently attenuates the stress wave, and the effect is positively correlated with porosity but negative with pulse time. Considering Figure 18 (b)-(c) and the impedance mismatch at the interface, a similar law was discovered that the transmission ratio increases with porosity and decreases with the rise of pulse time.

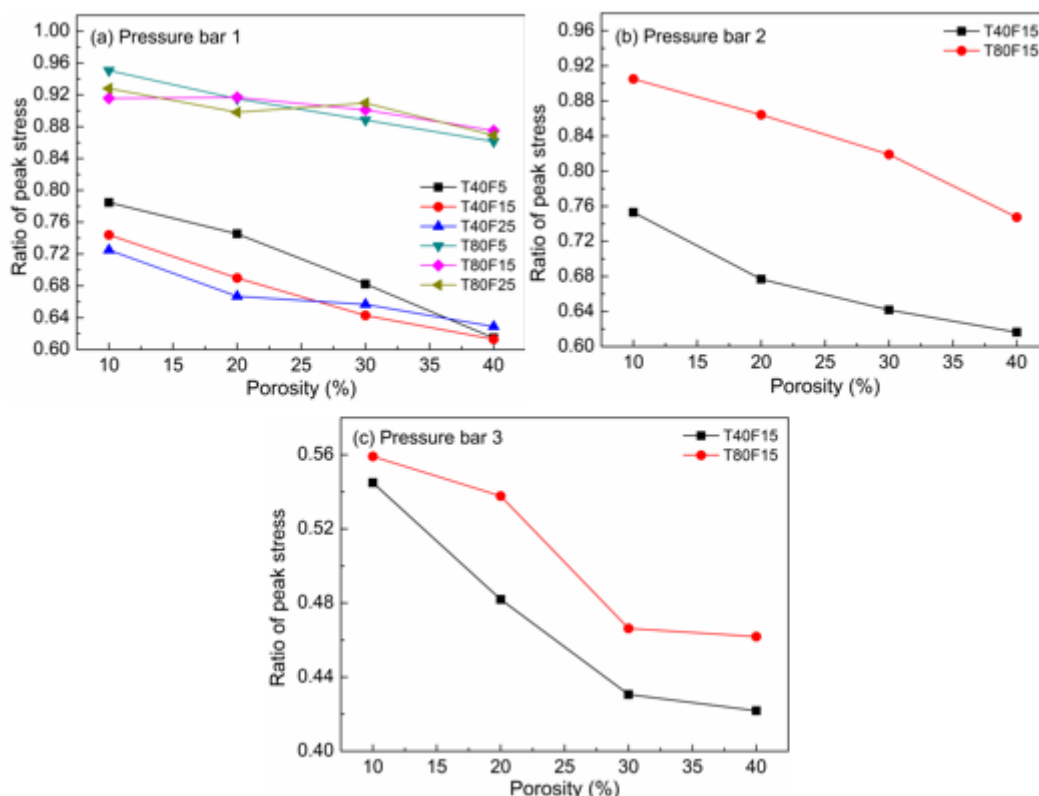


Fig.18. Ratio of transmitted peak stress

4.3.2 Influence of wave impedance ratio on transmission ratio

Based on two typical incident pulses, the author computed the peak stress ratios of the 3 pressure bars and various porous concrete specimens (Figure 19). The wave impedance ratios λ of the three types of interface were 1, 1.56 and 5.38 respectively for pressure bars 1, 2 and 3. It can be seen from Figure 19 that the transmission ratios decreased with the increase of the λ , especially for the incident stress wave T_{80F15} with a long pulse time. When $\lambda=1$, the minimum transmission ratio was 0.61 and 0.88 for T_{40F15} and T_{80F15} , respectively. However, when $\lambda=5.38$, the minimum transmission ratio was 0.61 and 0.88 for T_{40F15} and T_{80F15} , respectively. The wave attenuation effect of porous concrete, together with its adjustable wave impedance ratio, makes it possible to develop a multi-layered medium to effectively attenuate the stress wave in protective engineering.

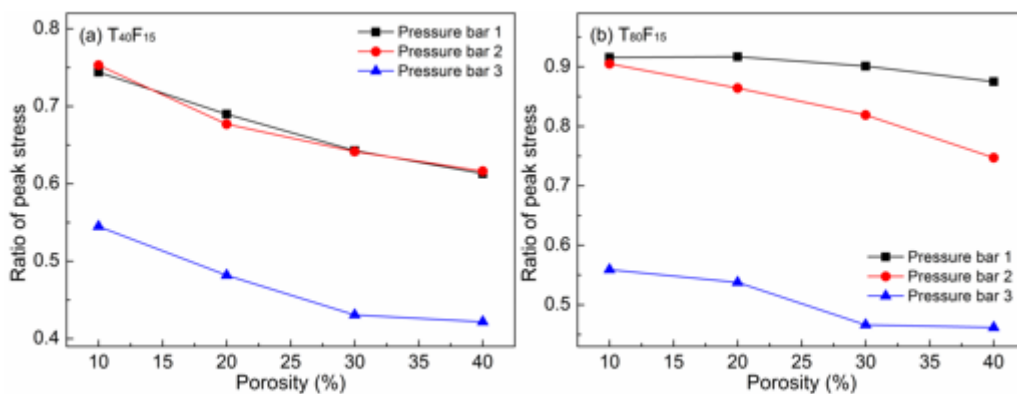


Fig.19. Ratio of transmitted peak stress of T_{40F15} and T_{80F15}

4.3.3 Dispersion effect of porous concrete

As shown in Figures 12-17, it is clear that almost all the transmitted stress waves bear certain degrees of dispersion: (1) the sharp corner of the triangle wave was smoothed and even flattened; (2) the rise time of stress waves was extended; (3) the transmitted stress wave exhibited obvious oscillations. Owing to the abundance of spherical inner pores with free surfaces, the plastic stress waves were reflected constantly at the interface between air and mortar. In addition with the unloading effect of elastic unloading wave, a few steps appeared in the steep front of the loading wave, leading to evident dispersion phenomena of time-history curve. Thus, it is concluded that the porous concrete has significant interface dispersion effect for stress wave.

Conclusion

To explore the lateral confinement effect and stress wave propagation, this paper establishes a numerical SHPB test model for the porous concrete fabricated with millimetre-size spherical saturated SAP. The conclusions are as follows.

(1) The extended Drucker-Prager model is a good choice for simulating the dynamic mechanical behaviours of porous concrete. The contribution of lateral confinement to the dynamic strength cannot be neglected. The strain-rate effect in the SHPB test is not merely the response of the material itself. Instead, it also involves the increment caused by the lateral inertial confinement effect. The strain-rate effect for high-porosity specimens is mainly resulted from the response of material itself. The influence of end friction effect on the compressive strength is more evident in high strain-rate scenarios and lower-porosity specimens.

(2) Low porosity specimens obtain more pronounced lateral inertial confinement effect and end face friction effect, while high porosity specimens exhibit stronger strain-rate effect caused by the concrete material itself.

(3) The porous concrete can effectively attenuate stress wave, especially in high porosity specimens, and the attenuation effect is positively proportional to the pulse time of stress wave. Meanwhile, the porous concrete can also lead to significant dispersion of stress waves, including constitutive dispersion and interface diffusion. The findings make it possible to create a multi-layer medium, with porous concrete as the interlayer, to guard against shock wave.

Acknowledgement

This work was supported by the Chongqing Science and Technology Commission, Chongqing, China (cstc2014jcyjA50026) and the Graduate Student Innovation Fund of Chongqing (CYB16127).

References

1. O.M. Jensen, P.F. Hansen, Water-entrained cement-based materials ☆: I. Principles and theoretical background, 2001, Cement & Concrete Research, vol. 31, no. 4, pp. 647-654.
2. O.M. Jensen, P.F. Hansen, Water-entrained cement-based materials ☆: ii. experimental observations, 2002, Cement & Concrete Research, vol. 32, no. 6, pp. 973-978.
3. K. Friedemann, F. Stallmach, J. Kärger, NMR diffusion and relaxation studies during cement hydration-a non-destructive approach for clarification of the mechanism of internal post

- curing of cementitious materials, 2006, *Cement & Concrete Research*, vol. 36, no. 5, pp. 817-826.
4. H. Cheng, Z. Cheng, Z. Pan, Super-absorbent polymer concrete and its preparation method, 2014, ZL201210345029.4 (Chinese patent).
 5. F. Wang, J. Yang, H. Cheng, J. Wu, X. Liang, Study on mechanism of desorption behavior of saturated superabsorbent polymers in concrete, 2015, *Aci Materials Journal*, vol. 112, no. 3.
 6. J. Yang, F. Z. Wang, Y. P. Liu, Comparison of ordinary pores with internal cured pores produced by superabsorbent polymers, 2015, *Advanced Materials Research*, vol. 1129, pp. 315-322.
 7. F. Wang, J. Yang, S. Hu, X. Li, H. Cheng, Influence of superabsorbent polymers on the surrounding cement paste, 2016, *Cement & Concrete Research*, vol. 81, pp. 112-121.
 8. Z. Deng, H. Cheng, Z. Wang, G. Zhu, H. Zhong, Compressive behavior of the cellular concrete utilizing millimeter-size spherical saturated sap under high strain-rate loading, 2016, *Construction & Building Materials*, vol. 119, pp. 96-106.
 9. Z. Deng, H. Cheng, Z. Wang, G. Zhu, Dynamic behavior and constitutive model of super absorbent polymer concrete under impact loading, 2015, *International Journal of Earth Sciences & Engineering*, vol. 8, no. 6, pp. 2974-2980.
 10. W.F. Brace, A.H. Jones, Comparison of uniaxial deformation in shock and static loading of three rocks, 2015, *Journal of Geophysical Research*, vol. 76, no. 20, pp. 26-29.
 11. W. Janach, The role of bulking in brittle failure of rocks under rapid compression, 1976, *International Journal of Rock Mechanics & Mining Sciences & Geomechanics Abstracts*, vol. 13, no. 6, pp. 177-186.
 12. L.A. Glenn, W. Janach, Failure of granite cylinders under impact loading, 1977, *International Journal of Fracture*, vol. 13, no. 3, pp. 301-317.
 13. C.N. Powell, Lateral inertia effects on rock failure in split Hopkinson bar experiments, 1979, *20th US Symposium on Rock Mechanics (USRMS)*.
 14. P.H. Bischoff, S.H. Perry, 1991, Compressive behaviour of concrete at high strain rates, *Materials & Structures*, vol. 24, no. 6, pp. 425-450.
 15. G. Cannistraro, M. Cannistraro, R. Restivo, The local media radiant temperature for the calculation of comfort in areas characterized by radiant surfaces, 2015, *International Journal of Heat and Technology* , vol. 33, no. 1, pp. 115-122.

16. F.K. Zeng, J. Tang, Z.J. Sang, H.L. Zhang, An experimental study on the stability bearing capacity of a new type of steel formwork, 2016, *Modelling, Measurement and Control B*, vol. 85, no. 1, pp. 186-197.
17. D.C. Drucker, W. Prager, Soil mechanics and plastic analysis or limit design, 2013, *Quarterly of Applied Mathematics*, vol. 10, no. 2, pp. 157-165.
18. Q.M. Li, H. Meng, About the dynamic strength enhancement of concrete-like materials in a split Hopkinson pressure bar test, 2003, *International Journal of Solids & Structures*, vol. 40, no. 2, pp. 343-360.
19. S. Yu, Y. Lu, Y. Cai, A numerical method to determine real strain-rate effect for rock-like materials, 2013, *Chinese Journal of Rock Mechanics & Engineering*, vol. 32, no. 6, pp. 3283-3290.
20. F. Qin, H. Jian, J.H. Zhang, C. Li, R. Zheng, Issues of SHPB test on concrete-like material, 2014, *Engineering Mechanics*, vol. 31, no. 5, pp. 1-14.
21. S. Chekroun, B. Abdelhadi, A. Benoudjit, Design optimization of induction motor using hybrid genetic algorithm "a critical analyze", 2016, *Advances in Modelling and Analysis C*, vol. 71, no. 1, pp. 1-23.
22. L.D. Bertholf, C.H. Karnes, Two-dimensional analysis of the split hopkinson pressure bar system, 1975, *Journal of the Mechanics & Physics of Solids*, vol. 23, no. 1, pp. 1-19.